

Modelling circumstellar discs with 3D radiation hydrodynamics

David M. Acreman, Tim J. Harries and David A. Rundle

School of Physics, University of Exeter, Stocker Road, Exeter EX4 4QL. E-mail acreman@astro.ex.ac.uk

31 July 2021

ABSTRACT

We present results from combining a grid-based radiative transfer code with a Smoothed Particle Hydrodynamics code to produce a flexible system for modelling radiation hydrodynamics. We use a benchmark model of a circumstellar disc to determine a robust method for constructing a gridded density distribution from SPH particles. The benchmark disc is then used to determine the accuracy of the radiative transfer results. We find that the SED and the temperature distribution within the disc are sensitive to the representation of the disc inner edge, which depends critically on both the grid and SPH resolution. The code is then used to model a circumstellar disc around a T-Tauri star. As the disc adjusts towards equilibrium vertical motions in the disc are induced resulting in scale height enhancements which intercept radiation from the central star. Vertical transport of radiation enables these perturbations to influence the mid-plane temperature of the disc. The vertical motions decay over time and the disc ultimately reaches a state of simultaneous hydrostatic and radiative equilibrium.

Key words: hydrodynamics – radiative transfer – methods: numerical

1 INTRODUCTION

Hydrodynamics calculations are used in investigations of a variety of problems associated with star formation, such as the collapse of protostellar cores (e.g. Goodwin et al. 2004), the fragmentation of protostellar discs (e.g. Boss 1997), and on the largest scale the gravo-turbulent collapse of a molecular cloud to form stars (e.g. Bate et al. 2003; Bate & Bonnell 2005).

Sophisticated as such calculations appear, the underlying physics regarding the thermal properties of the gas is much simplified. One of the usual approximations is the use of an equation of state (eos) in determining the pressure of the gas. An isothermal eos is often a good approximation in the most rarified regions, where the material is able to radiate, and thus cool, freely. The gas may be compressed adiabatically in the highest density regions, and a barotropic eos is sometimes adopted, with the polytropic exponent switching at a critical density in an attempt to reproduce the results of one-dimensional collapse calculations that incorporate radiative-transfer (Masunaga et al. 1998). The crucial point here is that the energy dumped into the cluster from accretion onto, and gravitation contraction of, the newly formed stars is neglected, and the radiation emitted by compressed gas (the ‘ $P dV$ ’ term) is assumed to escape without further interaction.

The solution is to include radiation-transfer self-consistently and perform a radiation-hydrodynamics (RHD) calculation. The simplest way to do this is to assume that the energy is transported by radiative diffusion of photons. The diffusion approximation is a good one at high optical depth, but breaks down in optically thin regions since the diffusion speed may exceed the speed of light as the mean-free-path tends to infinity; an essentially arbitrary flux limiter is adopted in this regime. Furthermore the approximation is often implemented as a grey method, typically using Rosseeland mean opacities tabulated as a function of temperature. Finally the diffusion approximation cannot treat the effects of shadowing, as the radiation field may diffuse around optically thick obstacles. The crucial advantage of the diffusion approximation though is of course speed: the radiation transport step is straightforward to implement and is not dominant in the RHD calculation. The first cluster collapse and disc fragmentation calculations using flux-limited diffusion have just started appearing in the literature (Boss 2008; Bate 2009b; Offner et al. 2009; Stamatellos & Whitworth 2009). The fundamental result of including a more complete thermal treatment is broadly in line with prior expectations i.e. the heating of the gas inhibits the fragmentation process.

Meanwhile dedicated radiation transfer (RT) codes have progressed far beyond the diffusion approximation and now take into account a wide array of processes such as poly-

arXiv:0912.2030v1 [astro-ph.SR] 10 Dec 2009

chromatic radiation transfer incorporating the radiation’s polarization state, multiple scattering, Mie phase matrices etc. These sophisticated RT codes have been employed to model cores (e.g. Stamatellos et al. 2005), discs (reviewed by Dullemond et al. 2007) and even entire clusters (Kurosawa et al. 2004). The principle barrier to using these codes in RHD is that of computation time, but the increase in CPU power and the adoption of parallelization mean that it is now feasible to conduct a full treatment of RT along with the hydrodynamics, thereby dropping the diffusion approximation.

This paper presents a method of coupling the TORUS radiative transfer code (Harries 2000) with the smoothed particle hydrodynamics (SPH) code of Bate (2009a). TORUS performs radiative transfer calculations using the Monte-Carlo method of Lucy (1999) with a diffusion approximation in regions of high optical depth. The radiative transfer calculations are performed on a grid which uses adaptive mesh refinement (AMR) to allow variable resolution. The SPH method is well suited to dealing with the large range in size scales encountered during star formation processes, hence an SPH code coupled to a Monte-Carlo radiative transfer code is a very flexible method for performing star formation calculations incorporating radiative feedback.

Accurately coupling the radiative transfer component to the SPH component requires an effective transformation from the Lagrangian particle description of SPH to the Eulerian grid description of an AMR grid. The procedure used for this transformation is tested using a circumstellar disc benchmark (see Sections 2 and 3). The temperature distribution and spectral energy distribution of the benchmark disc are examined in Section 4 in order to investigate how well the radiative transfer calculation works with the gridded density field and to understand the effects of grid and SPH spatial resolution. Finally the hybrid code is tested under realistic conditions via a simulation of a circumstellar disc around a T Tauri star (Section 5).

2 CIRCUMSTELLAR DISC BENCHMARK

The accuracy of the SPH method has previously been examined in detail (e.g. Price (2008) and references therein) so we do not attempt to benchmark the SPH component of the code here. Likewise the TORUS radiative transfer code has also been benchmarked elsewhere (Pinte et al. 2009). Consequently we can be confident in the accuracy of the SPH and radiative transfer codes individually and we instead focus on the accuracy of the mechanism by which they are coupled. The benchmark case presented here is therefore a ‘static’ benchmark in which we represent an analytical density distribution with SPH particles and test whether the radiative transfer code can calculate accurate results using this SPH density representation.

In the absence of an analytical test case, benchmarking of codes used for calculating radiative transfer in circumstellar discs is carried out by code comparison studies (Pascucci et al. 2004; Pinte et al. 2009). We base our SPH disc benchmark on the axisymmetric circumstellar disc of Pascucci et al. (2004). Representing a structure with rotational symmetry using a 3D geometry allows us to validate the operation of our method against well tested results from

other codes while fully exercising the 3D capabilities of our own system. The geometry is a stringent test of the gridding method, since it contains a large range in linear scales that need to be resolved, and sharp density gradients (in particular the disc inner edge).

The density of the disc benchmark described by Pascucci et al. (2004) is given by

$$\rho(r, z) = \rho_0 \left(\frac{r}{r_d}\right)^{-1} \exp\left(-\frac{\pi}{4} \left(\frac{z}{h(r)}\right)^2\right) \quad (1)$$

where r is the distance from the central star in the mid-plane and z is the height from the mid-plane. The expression $h(r)$ is given by

$$h(r) = z_d \left(\frac{r}{r_d}\right)^{1.125} \quad (2)$$

and ρ_0 , z_d and r_d are constant parameters. The definition of $h(r)$ is the definition used by Pascucci et al. (2004) which differs from the standard scale height definition (used later in this paper) by a factor of $\frac{\pi}{2}$. We base our benchmark model on the most optically thick case presented by Pascucci et al. (2004) which has a mid-plane optical depth of $\tau = 100$ at $\lambda = 550$ nm and a mass of $0.011 M_\odot$. This requires $r_d = 500$ au, $z_d = 0.25r_d$ and $\rho_0 = 8.1614 \times 10^{-18} \text{ g cm}^{-3}$, with the disc truncated at an outer radius of 1000 au and an inner radius of 1 au. The disc is irradiated by a solar-type star with a black body spectrum.

The benchmark disc is implemented using an ensemble of equal mass SPH particles. If all the particles have the same mass then the number density is proportional to the mass density, hence the SPH particles sample a probability density distribution such that the probability of finding a particle in a given volume is proportional to the mass in that volume as a fraction of the total mass (Gingold & Monaghan 1977). Hence the analytical density function can be converted into a probability function which describes the probability of finding a particle in a given volume. An ensemble of particle positions can then be calculated by randomly sampling the probability density functions for r and z and assigning a uniformly random azimuthal angle ϕ . The particle’s density is set to the value given by Eqn 1 based on the particle’s position.

Each particle is assigned a smoothing length h_{smooth} given by

$$h_{\text{smooth}} = 1.2 \left(\frac{m_{\text{part}}}{\rho_{\text{part}}}\right)^{1/3} \quad (3)$$

where m_{part} is the particle mass and ρ_{part} is the particle density, according to the method of Price & Bate (2007). The smoothing length is used when reconstructing properties represented by the ensemble of particles, for example the density distribution on the radiative transfer grid (see Section 3).

3 GENERATION OF AN ADAPTIVE GRID FROM SPH PARTICLES

An important step in setting up grid-based radiative transfer using a density distribution derived from SPH particles is determining an effective transformation from the Lagrangian

particle description to the Eulerian grid description. The representation on grid should preserve important properties of the SPH model (e.g. total mass) but also needs to take account of the possibility that a radiative transfer calculation requires the highest resolution in different regions to a hydrodynamics calculation (e.g. to resolve opacity gradients). This section determines a grid construction method which allows a good degree of control over the number of cells in the grid, and the location of the highest resolution regions, while maintaining an accurate representation of the total disc mass.

3.1 Grid generation method

TORUS uses an adaptive grid based on the octree method. In a 3D geometry the initial grid comprises 8 cells (one octal) with 2 cells in each dimension. An algorithm is applied to determine whether to split each cell into a further 8 cells, similar to the method of Kurosawa & Hillier (2001). The properties of the adaptive grid are determined by a combination of the algorithm used to decide when to split a cell and the method used to assign density values to cells.

The density in a given grid cell is calculated using an exponential kernel smooth. If the sum of the kernel weights is greater than 0.3 the density is normalised by the sum of the kernel weights, to ensure a smooth density distribution within the interior of the disc. If the sum of the weights is less than 0.3 then the density is not normalised by the sum of the weights, in order to avoid numerical effects at the free surface, as described by Price (2007). For more details of the algorithm used to generate the AMR grid from SPH particles see Rundle & Harries (2009).

3.2 Cartesian grid generation tests

Two grid splitting conditions were tested. The first method splits a grid cell if the mass within the cell exceeds a given limit. For this condition the resolution is highest where the density is highest and the grid cell size is analogous to the SPH particle smoothing length. The second condition decides whether to split the cell based on the fractional density difference between the most dense and least dense SPH particles contained within the cell. The quantity

$$f_{\text{split}} = \frac{\rho_{\text{max}} - \rho_{\text{min}}}{\rho_{\text{max}} + \rho_{\text{min}}} \quad (4)$$

is calculated, where ρ_{max} is the highest SPH particle density and ρ_{min} is the lowest SPH particle density, and the cell is split if a specified value of f_{split} is exceeded. The first condition gives a resolution like that of the original SPH representation whereas the second condition should better represent gradients in density which are important for radiative transfer calculations.

To illustrate the effects of the different splitting methods two example grids are shown in Fig. 1. A grid constructed from 10^7 particles, using a mass per cell limit of 5×10^{26} g, is plotted in Fig. 1(a). This plot is a slice perpendicular to the disc mid-plane and shows increased resolution towards the disc centre and mid-plane where the density is higher. A grid with $f_{\text{split}} = 0.1$, also using 10^7 particles, is plotted in Fig. 1(b). The resolution increases towards the edge of the disc, where there are large density gradients, and

also increases towards the centre of the disc. When the density split condition is used there is a noticeable asymmetry to the grid resolution, due to statistical fluctuations in the SPH particle distribution. The effect is seen more readily with the density split condition because the grid resolution is being enhanced in lower density regions, where SPH particles sample the density distribution less well than in high density regions.

For each splitting condition a number of AMR grids were generated using different values of the mass per cell limit or f_{split} . This was repeated for discs represented by 10^5 , 10^6 and 10^7 SPH particles. Figure 2 plots the number of octals generated as a function of mass per cell or f_{split} (solid line), and the percentage error in the disc mass (dashed line). The percentage error in disc mass is calculated by comparing the total mass on the AMR grid with the known mass of $0.011 M_{\odot}$ based on the analytical form of the density distribution, and a positive value indicates that mass on the grid is too large.

The mass per cell condition allows a wide range in the total number of octals while maintaining a total mass which is correct to within a few percent. The number of octals as a function of mass per cell limit is consistent between runs with different numbers of SPH particles, apart from the case with 10^5 particles and a mass limit of 10^{26} g. In this case the mass per cell limit is smaller than the SPH particle mass and the grid is over sampling the SPH resolution. In the other cases the mass per cell limit is greater than the SPH particle mass. For mass per cell limits of 10^{28} g and less the total mass error varies only slowly as a function of mass per cell and is accurate to within a few percent. There is a positive bias in the total mass but using more SPH particles results in a more accurate total mass.

If a density contrast condition is used then the total number of octals depends on the number of particles, unlike in the mass per cell case. The general form of the number of octals as a function of density contrast is the same in all three cases but the normalisation varies substantially. In order to ensure a total mass accurate to with 1 per cent the density contrast condition would require at least 10^7 particles and a density contrast threshold of no more than 0.3.

The density contrast condition is effective in adding extra resolution in regions of high density contrast which are likely to be important in radiative transfer calculations. However this condition has a less robust total mass representation than the mass per cell limit. By using a combination of these two conditions it is possible to add extra resolution in high contrast regions and still maintain an accurate total mass.

3.3 Cylindrical polar grid generation

For some geometries it may be appropriate to use a cylindrical polar co-ordinate system. A mass per cell splitting condition can still be used but needs to be modified to take into account that for fixed values of dr and dz the cell volume increases as cylindrical polar radius increases. Consider a Cartesian grid with cubic volume elements and let

$$dl_{\text{cart}} = dx = dy = dz \quad (5)$$

so that

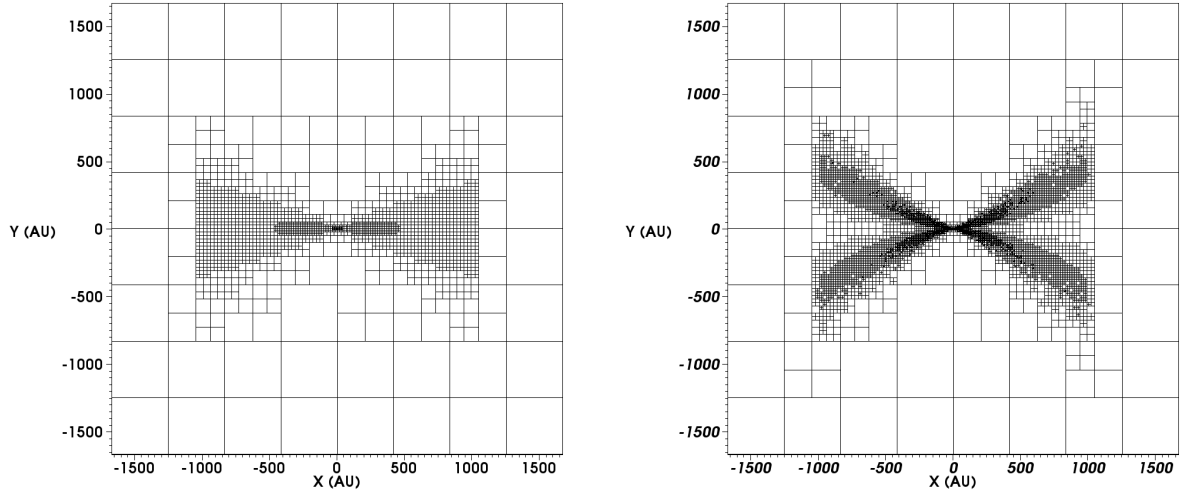
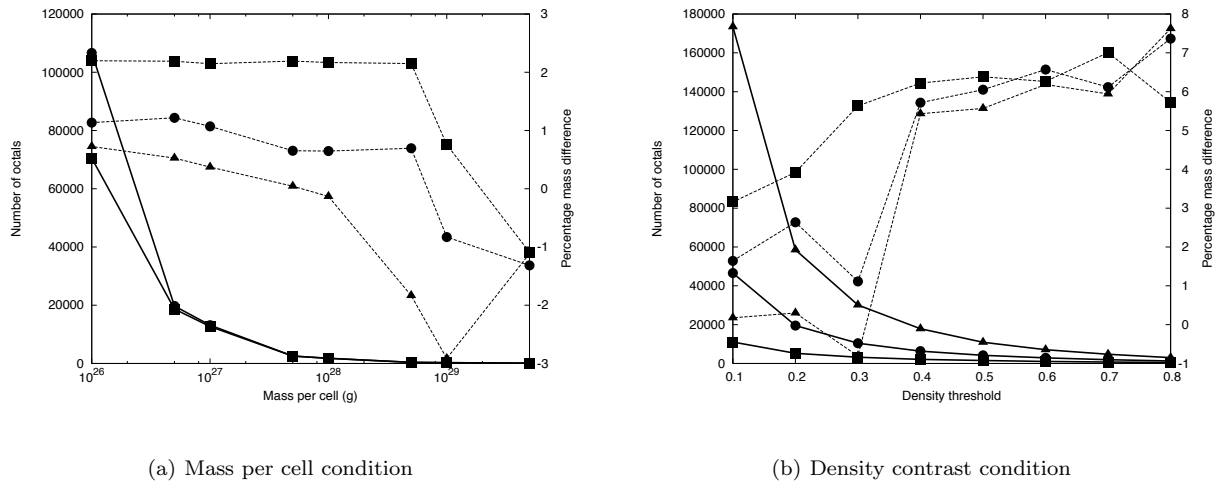

 (a) AMR grid with a mass per cell condition of 5×10^{26} g. (b) AMR grid with a density condition of $f_{\text{split}} = 0.1$.

Figure 1. Example AMR grids for a mass per cell splitting condition of 5×10^{26} g (left) and a density contrast splitting condition of $f_{\text{split}} = 0.1$ (right) constructed from 10^7 SPH particles. The grids are slices perpendicular to the disc mid-plane.


(a) Mass per cell condition

(b) Density contrast condition

Figure 2. Number of octals (solid line) and percentage error in total disc mass (dashed line) for the benchmark disc represented on Cartesian AMR grids. The grids were generated using either a mass per cell limit (left) or density contrast limit (right) and different numbers of particles (10^5 , 10^6 or 10^7). Results using 10^5 particles are plotted with squares, 10^6 particles with circles and 10^7 particles with triangles. The number of octals for a mass per cell condition with 10^7 particles is not plotted as it is indistinguishable from the case with 10^6 particles.

$$dl_{\text{cart}} = \left(\frac{dM_{\text{cart}}}{\rho_{\text{cell}}} \right)^{1/3} \quad (6)$$

where dM_{cart} is the mass of a cell in the Cartesian grid and ρ_{cell} is the density of the cell. In a cylindrical polar grid the mass of a cell is given by

$$dM_{\text{cyl}} = \rho_{\text{cell}} \frac{2\pi r dr dz}{n_{\text{az}}} \quad (7)$$

if there are n_{az} uniform azimuthal cells. If the resolution in r and z is the same then we can define

$$dl_{\text{cyl}} = dr = dz \quad (8)$$

which is related to the cell mass and density by

$$dl_{\text{cyl}} = \left(\frac{n_{\text{az}} dM_{\text{cyl}}}{2\pi r \rho_{\text{cell}}} \right)^{1/2} \quad (9)$$

If we require the resolution in cylindrical polar r and z to match the resolution in Cartesian x , y and z then $dl_{\text{cyl}} = dl_{\text{cart}}$. From eqn 6 and 9

$$dM_{\text{cyl}} = \frac{2\pi r}{n_{\text{az}}} \rho^{1/3} dM_{\text{cart}}^{2/3} \quad (10)$$

which describes the required conversion from a mass per cell limit suitable for a Cartesian grid (dM_{cart}) to an equivalent mass per cell limit suitable for a cylindrical polar grid (dM_{cyl}).

The grid generation tests were run using a cylindrical polar geometry with the modified mass per cell limit described above and an unmodified density contrast condition. The results are plotted in Fig. 3. Using a cylindrical polar geometry results in a significantly reduced number of octants in the AMR grid but with larger mass errors. Provided the mass per cell limit is no more than 10^{27} g then the total mass is well represented with significantly fewer cells than in a Cartesian grid. The density contrast condition alone does not represent the total mass to within 3% accuracy even with $f_{\text{split}} = 0.1$. Although this condition successfully adds enhanced resolution in regions of higher density contrast it needs to be combined with a mass per cell limit to ensure a robust total mass representation.

4 COMPARISON OF TEMPERATURE DISTRIBUTION AND SEDS WITH BENCHMARK RESULTS

Having investigated the procedure for setting up the radiative transfer grid we now proceed to studying the accuracy of the results from the radiative transfer calculation. This was carried out by comparing temperature distributions and spectral energy distributions (SEDs) from the benchmark disc. Temperature distribution errors provide a clear picture of where errors in the radiative transfer calculation are located whereas SEDs provide a direct link to an observable quantity and are a stringent test of the accuracy of the radiative transfer calculation. The key problem here is that the resolution necessary for adequately describing the fluid flow is not necessarily the same as required for accurately modelling the radiation field.

The disc was initially modelled using 10^5 SPH particles with an AMR grid constructed from a mass per cell limit of 5×10^{26} g. This number of SPH particles would normally be considered as sufficient to adequately represent a disc of this mass in a purely hydrodynamical calculation. The mass per cell limit was chosen in preference to the density contrast limit to give the highest resolution near the central region of the disc, which we expect to be most important for determining the temperature of the disc at the inner edge and the SED.

In Fig. 4 we plot the fractional error in the temperature distribution at radiative equilibrium for the benchmark disc. TORUS calculates the temperature distribution using a high resolution 2D geometry, in order to determine the correct temperature as a function of cylindrical polar r and z coordinates. This is then compared to the temperature from the SPH disc for each SPH particle. Positive values of the fractional error indicate that the SPH disc is hotter than the expected value. The temperatures show deviations of -30%

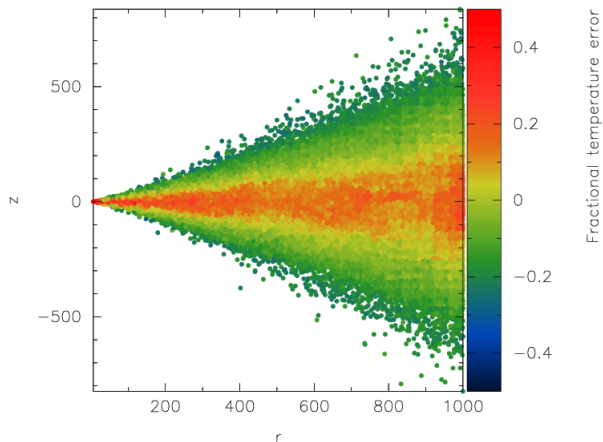


Figure 4. Fractional errors in the temperature distribution of a 10^5 particle disc. The radiative transfer grid is a Cartesian grid generated using a mass per cell limit of 5×10^{26} g. Axis units are au.

to $+50\%$ from the benchmark values, a deviation that is purely driven by the resolution of the density field derived from the SPH particles, since a ‘TORUS only’ calculation, where the AMR grid is refined on optical depth criteria and the cell densities are found from the analytical description of the density structure (Eqn. 1), matches the benchmark temperatures to within 2%. The systematic differences in the temperature distribution are due to an increased vertical transport of radiation from the surface layers of the disc to the mid-plane due to a lack of spatial resolution, leading to errors in the calculation of the specific intensities (particularly in the inner disc region). These systematic differences are more readily apparent in the emergent SEDs, which are a more sensitive probe of the accuracy of the RT calculation than the temperature distribution.

SEDs were calculated using the TORUS code for viewing angles of 12.5 and 77.5 degrees (where an inclination angle of zero degrees indicates that the disc is viewed face-on) and the results are plotted in Fig. 5 (dashed line). Also plotted in Fig. 5 are the benchmark results of Pascucci et al. (2004) (solid line). Both SEDs show significant departures from the benchmark results; there is excess emission between 10-100 μm and at a viewing angle of 77.5 degrees there is also a significant reduction in flux below 1 μm . Both these discrepancies are attributable to a lack of resolution within a few au of the central object. The density distribution in the central region of this disc is plotted in Fig. 6 which shows that the central 1 au gap is not represented. There are two effects in operation; firstly the grid resolution in this region is larger than 1 au and secondly the smoothing lengths of the particles are larger than 1 au. In order to correctly represent the central gap there needs to be higher grid resolution around the central source and more SPH particles are required so that the smoothing lengths are smaller.

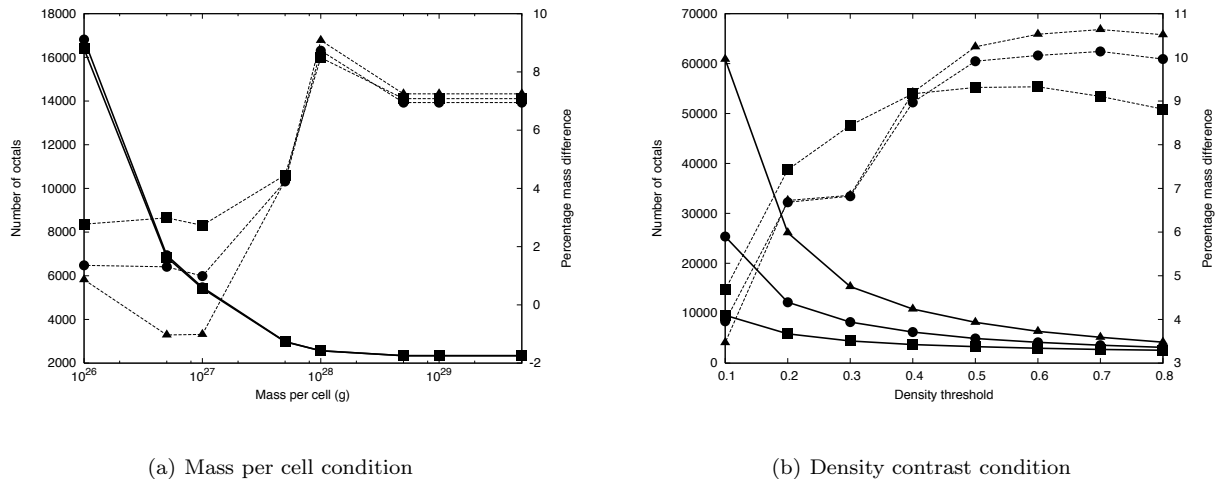


Figure 3. Number of octals (solid line) and percentage error in total disc mass (dashed line) for the benchmark disc represented on cylindrical polar AMR grids. The grids were generated using either a mass per cell limit (left) or density contrast limit (right) and different numbers of particles (10^5 , 10^6 or 10^7). Results using 10^5 particles are plotted with squares, 10^6 particles with circles and 10^7 particles with triangles. The number of octals for a mass per cell condition with 10^7 particles is not plotted as it is indistinguishable from the case with 10^6 particles.

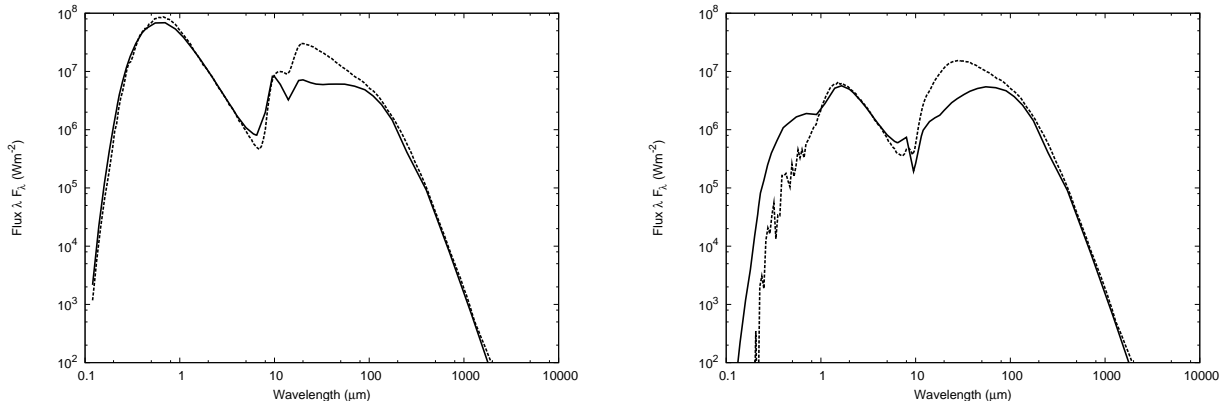


Figure 5. SEDs from the benchmark disc represented by 10^5 particles and a Cartesian radiative transfer grid generated using a mass per cell limit of 5×10^{26} g. SEDs are shown for inclination angles of 12.5 degrees (left) and 77.5 degrees (right). The benchmark SED is plotted as a solid line and the TORUS SED is plotted as a dashed line. The corresponding fractional temperature errors are plotted in Fig. 4.

4.1 Grid resolution

Decreasing the mass per cell limit to achieve the required resolution around the central source would result in too many cells being generated in other regions of the disc. In order to achieve a grid resolution of less than 1 au around the source it was necessary to specify additional criteria for refining the grid. Three cubes of increased resolution were added to the AMR grid with sizes 1.5×10^{15} cm, 3×10^{14} cm and 6×10^{13} cm. Within each cube it was required that the cell size be no larger than 0.1 of the cube dimension. In order to confirm that the grid modifications provide sufficient resolution to generate an accurate SED three calculations were performed with the central part of the disc forced to the cor-

rect density values from the analytical density description. A spherical region with radius 1.0×10^{15} cm, 5.0×10^{14} cm or 2.5×10^{14} cm was over written with the benchmark disc density after the initial grid generation was performed. The resulting SEDs are plotted in Fig. 7. The solid line shows the benchmark result and the other lines show SEDs for forcing regions of radius 1.0×10^{15} cm (long dashed line), 5.0×10^{14} cm (short dashed line) and 2.5×10^{14} cm (dotted line). With the correct density forced out to a radius of 1.0×10^{15} cm the SED is close to the benchmark result for both viewing angles, however if the forced region is reduced in size there is a significant discrepancy relative to the benchmark SED. This confirms that the grid now has

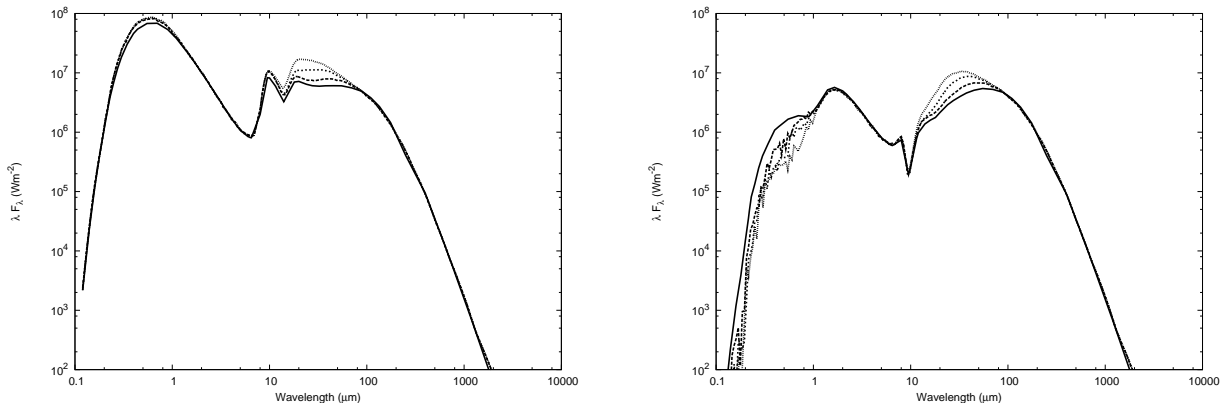


Figure 7. SEDs from the benchmark disc represented by 10^5 particles and a Cartesian radiative transfer grid generated using a mass per cell limit of 5×10^{26} g. Extra resolution has been added around the central source and the TORUS density distribution is forced to the correct value within a radius of 1.0×10^{15} cm (long dashed line), 5.0×10^{14} cm (short dashed line) and 2.5×10^{14} cm (dotted line). SEDs are shown for inclination angles of 12.5 degrees (left) and 77.5 degrees (right) with the benchmark result plotted as a solid line.

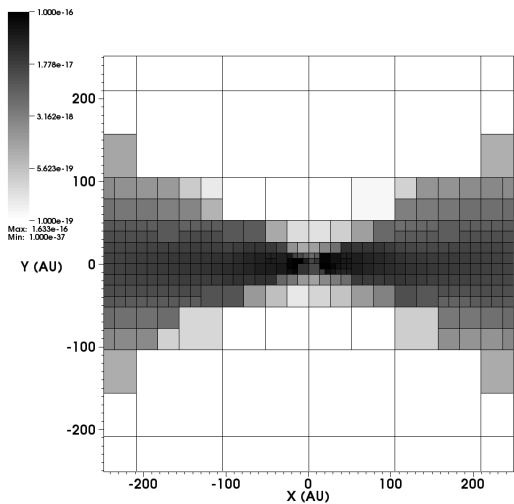


Figure 6. Density (g cm^{-3}) in the central region of the benchmark disc represented by 10^5 particles and a Cartesian radiative transfer grid generated using a mass per cell limit of 5×10^{26} g. The central 1 au gap is not represented and the effects on the temperature distribution and emergent SEDs are shown in Fig. 4 and Fig. 5 respectively.

enough resolution to generate an accurate SED but also indicates that using 10^5 particles does not give a sufficiently accurate density distribution within the central 1.0×10^{15} cm of the disc.

4.2 Number of particles

Further calculations were performed using different numbers of SPH particles and the enhanced grid resolution described above in order to determine the impact of the number of SPH particles on the accuracy of the radiative transfer calculation. The density distribution in the central region of

the disc is plotted in Fig. 8 in order to show how the representation improves as the number of particles is increased. The effective resolution of the AMR mesh is dependent on two factors; the probability of having sufficient particles to adequately sample the small volume of the disc inner-edge, and the particle smoothing length (which determines the effective spatial resolution of the SPH density representation). With 10^5 and 10^6 particles a central gap is present but is too large. With 10^7 particles there is more material close in to the source but the gap itself is not represented (because the smoothing length of the particles near the disc inner-edge is too large) and the source is obscured. Only with 10^8 particles is a gap of approximately the correct size present. The representation of the central 1 au gap is significantly affected by the number of particles used to represent the disc, with a large number of particles required to achieve an accurate density distribution in this spatially small region.

Figure 9 shows fractional errors in the temperature distribution for different numbers of particles. When using 10^5 particles to represent the disc there is a too much heating in the disc mid plane and insufficient heating further out of the mid plane. The effect is reduced as the number of particles is increased and reaches a very low level with 10^8 particles, at which stage the temperature distribution agrees with the benchmark to within $\sim 10\%$.

To allow a more quantitative comparison the mid-plane temperature and the benchmark mid-plane temperature are plotted in Fig. 10 for all particles within 0.01 scale heights of the mid-plane. The fractional temperature error for each particle is also plotted where a positive error indicates a temperature hotter than the benchmark value.

SEDs are plotted in Fig. 11 for a viewing angle of 12.5 degrees and Fig. 12 for a viewing angle of 77.5 degrees. At the shortest wavelengths the 12.5 degrees inclination angle SED is dominated by the photosphere of the central star. This region of the SED is well represented with 10^5 and 10^8 particles but is of course less well represented with 10^6 or 10^7 particles where the central star is obscured. At the longest wavelengths the disc is optically thin and the SEDs

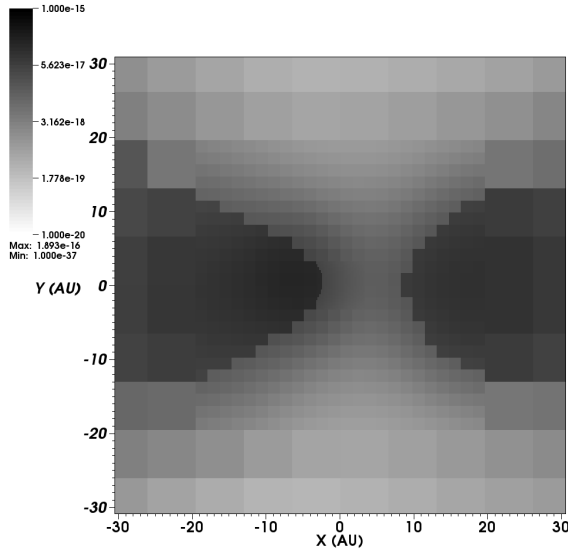
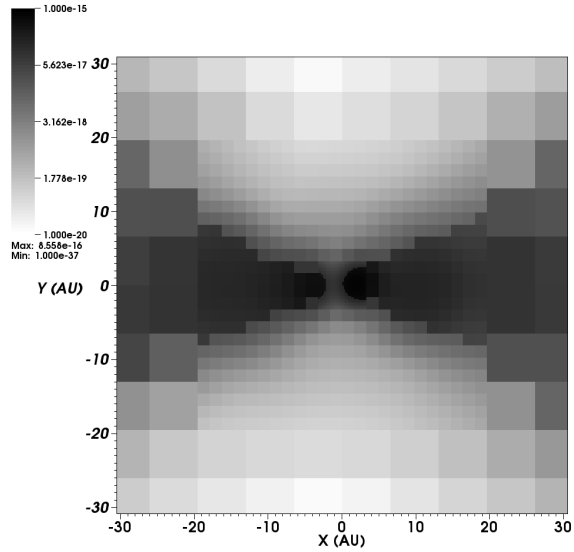
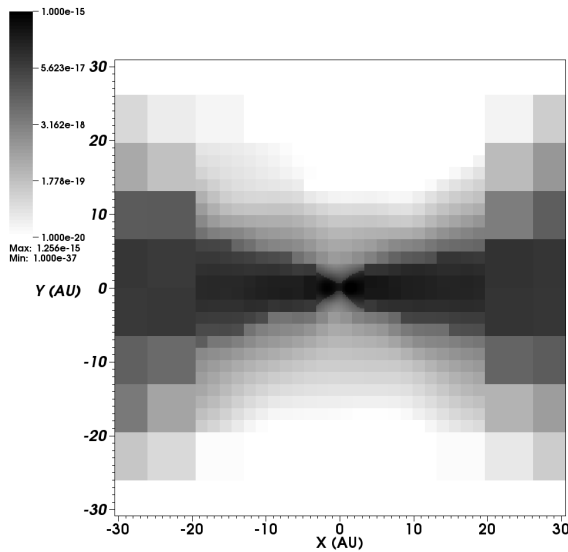
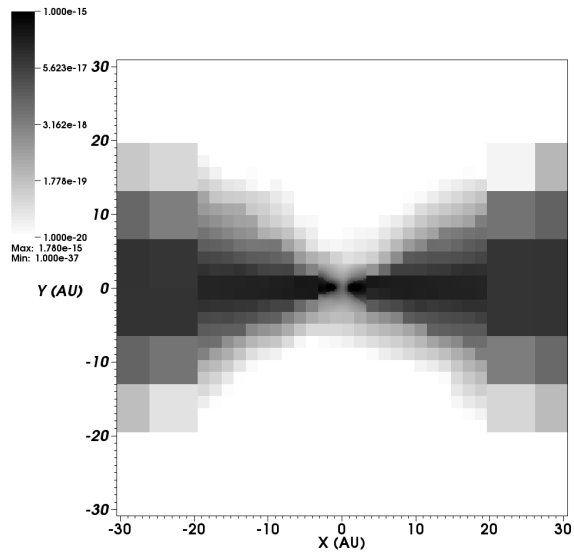
(a) 10^5 particles(b) 10^6 particles(c) 10^7 particles(d) 10^8 particles

Figure 8. Density (g cm^{-3}) in the central region of the disc as represented on AMR grids derived from different numbers of SPH particles. The AMR grid is generated using a mass per cell limit of 5×10^{26} g with extra resolution at the origin as described in Section 4.1.

will be well modelled provided the total disc mass is accurately represented. In all four cases the total disc mass is well represented (see Section 3) and the long wavelength SED matches the benchmark results. At intermediate wavelengths the SED is sensitive to the details of the disc representation and it is clear that accurately modelling the SED from this disc is challenging, even with 10^8 particles. At an inclination angle of 77.5 degrees the central star is overly obscured by disc material. If the spatial resolution at the inner edge is low then the inner edge will be too thick (in the z direction) and too close to the central star. As a result there will be overly dense material in the observer's line of sight.

An SED with insufficient emission from the central star at this inclination angle is indicative that the inner edge is not well resolved.

The results of our benchmark tests have shown that the temperature distribution within the disc can be calculated with a typical accuracy of better than 20 per cent with only 10^6 particles (see Fig. 9 and Fig. 10), which offers a significant improvement over the use temperatures derived from an eos. Although relatively few particles are required to give a temperature distribution sufficiently accurate for hydrodynamic calculations, obtaining an accurate SED from the model disc would require many more particles, as there

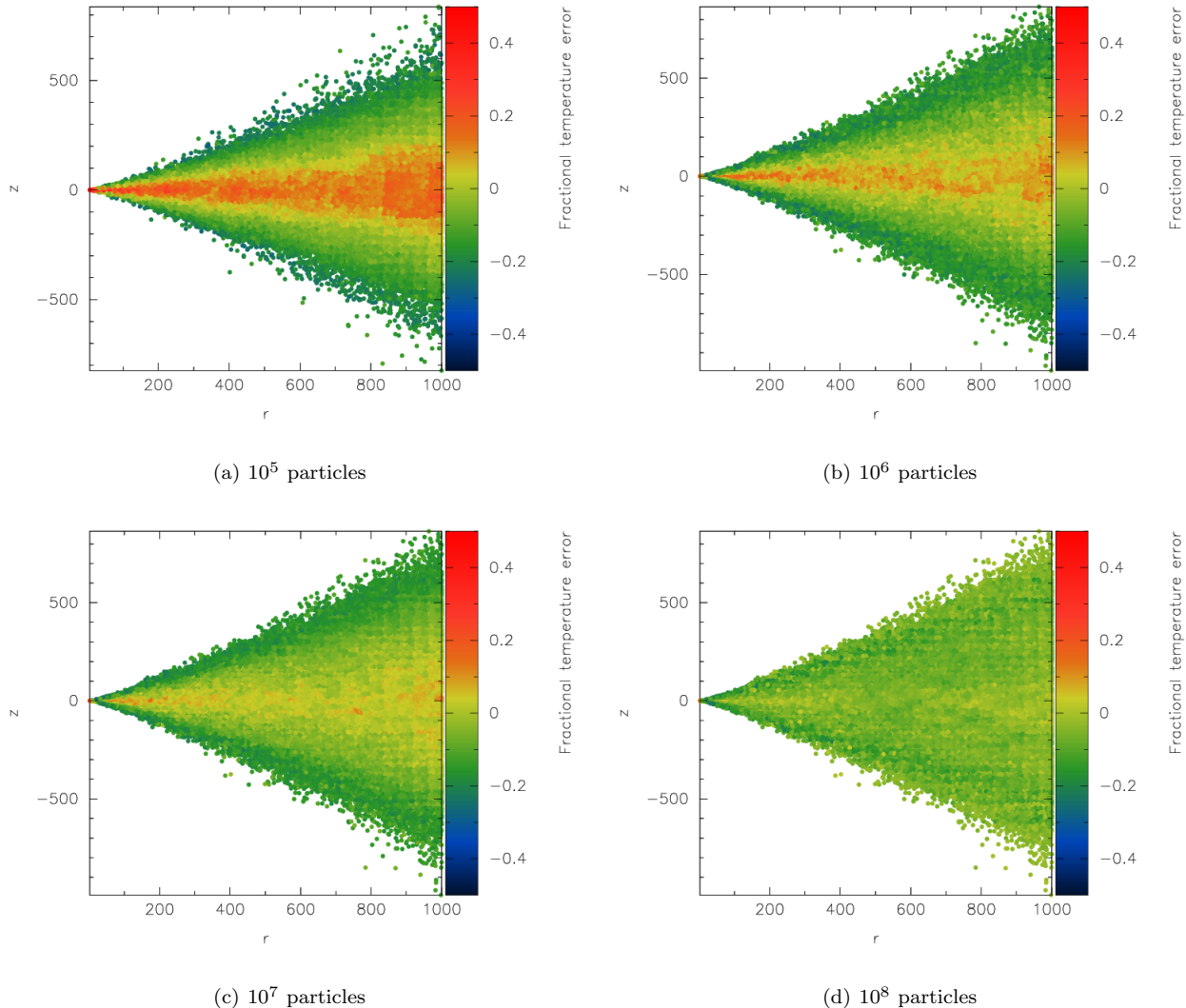


Figure 9. Fractional errors in the temperature distribution of discs represented by 10^5 , 10^6 , 10^7 and 10^8 particles. The AMR grid is generated using a mass per cell limit of 5×10^{26} g with extra resolution at the origin as described in Section 4.1. The axis units are au. The corresponding density distributions in the central part of the disc are plotted in Fig. 8.

are significant discrepancies relative to the benchmark even with 10^8 particles (see Fig. 11 and Fig. 12).

5 COUPLED SPH AND MONTE-CARLO RADIATIVE TRANSFER SIMULATION OF A CIRCUMSTELLAR DISC

The above analysis indicates that the hybrid code is capable of successfully passing the density distribution from the hydrodynamics step to the radiative-transfer code, and that temperatures sufficiently accurate for hydrodynamic calculations (under the assumption of radiative equilibrium) can be passed back to the SPH code in order to update the gas pressure and perform the next hydrodynamical step. In order to test the feasibility of performing a radiation-hydrodynamics calculation using the hybrid code we adopt a ‘realistic’ test problem, that of a circumstellar disc around a classical T Tauri star. The mid-plane optical depths here

are higher than that of the Pascucci benchmark, providing a more demanding challenge both in terms of computation time and required numerical accuracy.

5.1 Description of model

A model system was constructed similar to the classical T Tauri star AA Tau. O’Sullivan et al. (2005) determine the properties of AA Tau using Monte-Carlo modelling of the observed SED, and we use these derived properties as a basis for constructing our model system. The disc of $0.02 M_{\odot}$ is initialised with an outer radius of 150 au, and an inner radius of 1.0 au. The inner radius of our model disc is enlarged, compared to the inner radius determined by O’Sullivan et al. (2005), as resolving a smaller inner edge in a disc of this size would require many more SPH particles. The inner edge of our model disc will be cooler than the inner edge of a disc with a smaller radius but the important physical processes are captured (i.e. there is an optically thick inner edge which

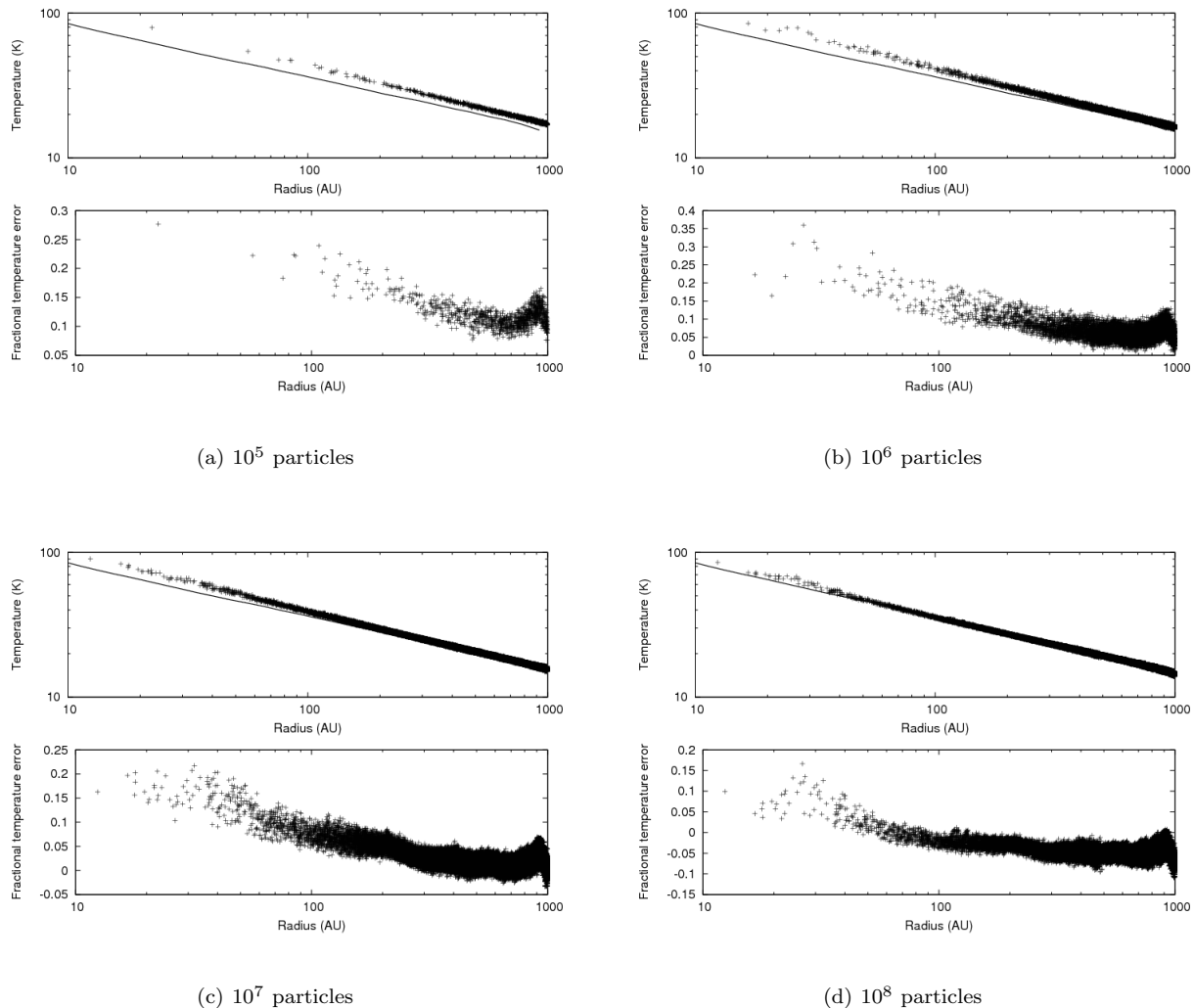


Figure 10. Fractional temperature error, as a function of radius, for particles within 0.01 scale heights of the mid-plane for discs represented by 10^5 , 10^6 , 10^7 and 10^8 particles.

can puff up and shadow the disc causing a hydrodynamic response.) The central star has a mass of mass $1 M_{\odot}$ and is represented by a sink particle which accretes gas particles within an accretion radius of 1.0 au. The disc itself is initially represented using 10^6 particles of equal mass, although some of these particles are accreted by the central sink particle as the simulation progresses. The central star has a radius of $2 R_{\odot}$, a temperature of 4000 K and a luminosity of $0.9 L_{\odot}$. The source spectrum taken to be a black body.

The disc is initially evolved using only the SPH part of the code in order to bring the disc into dynamical equilibrium. The SPH implementation is that described by Price & Bate (2007) which uses the variable smoothing length formulation given in eqn 3. Density and smoothing length are calculated iteratively according to the method of Price & Monaghan (2007) with approximately 60 neighbours on average. An artificial viscosity term is calculated using the scheme described by Monaghan (1992) with parameters $\alpha = 1$ and $\beta = 2$. During this initial phase the internal energies of the SPH particles are determined using an equation of state

which is isothermal perpendicular to the plane of the disc and has a $T \propto 1/r$ radial dependence. The disc is evolved for approximately 4000 years of simulated time in order to allow transient effects from the initialisation to dissipate. As the disc settles towards an equilibrium state there are vertical motions which cause fluctuations in the envelope of the disc, with the inner regions of the disc reaching equilibrium more rapidly than the outer regions.

The disc is then evolved using the combined SPH and radiative transfer code. In this configuration the internal energies of the SPH particles are set using the temperatures calculated by the radiative transfer code. The SPH part of the code does not change the particle temperatures and they retain the temperature assigned by the radiative transfer code until the next radiation time step. The temperatures calculated by the radiative transfer code are equilibrium temperatures, as it is assumed that the time scale for radiative equilibrium is short compared to the dynamical time scale of the disc (i.e. the “prompt escape” regime described by Nayakshin et al. 2009). Calculating temper-

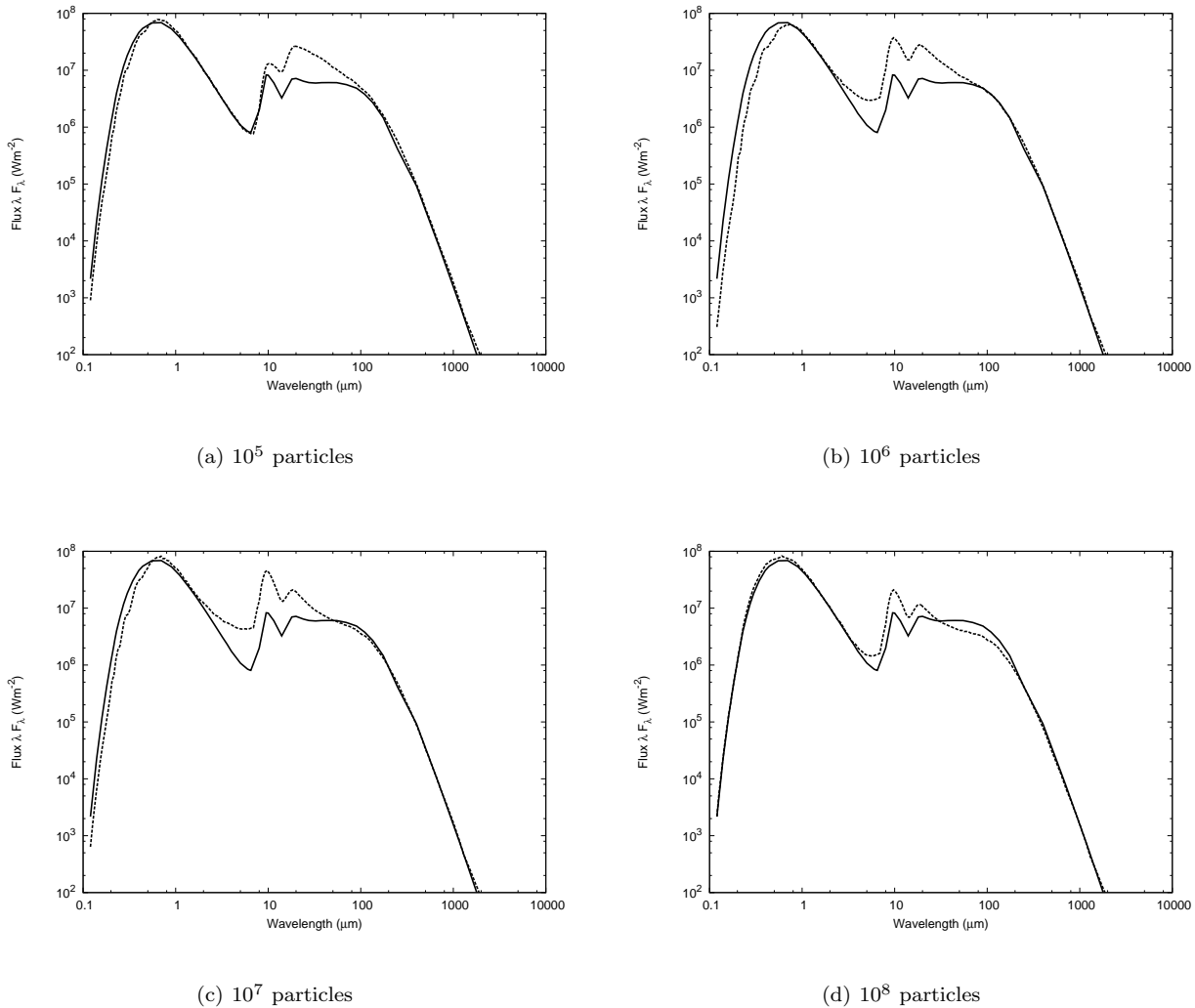


Figure 11. SEDs at a 12.5 degree inclination angle for discs represented by 10^5 , 10^6 , 10^7 and 10^8 particles. The benchmark result is plotted as a solid line and the TORUS SEDs are plotted as dashed lines. The corresponding density distributions in the central part of the disc are plotted in Fig. 8 and fractional temperature errors are plotted in Fig. 9.

atures from the radiative transfer scheme alone is only a valid approximation provided heating from stellar radiation dominates other sources of heating (e.g. viscous or shock heating). The addition of a time dependent radiative transfer scheme would allow for the inclusion of additional (non-stellar) sources of heating, such as adiabatic compression, but is beyond the scope of this work.

The frequency with which the radiative transfer is calculated is determined by the sound crossing time in the inner regions of the disc as this is the time scale over which the scale height in this region will vary and effect the transfer of radiation into the outer parts of the disc. The vertical sound crossing time at a radius of 10 au is typically approximately 2 years, so a radiative transfer calculation is performed after every four hydrodynamics time steps (equivalent to every 2.4 years).

A cylindrical polar grid, with adaptive r and z cells was used for the radiative transfer step. The cells were split in the azimuthal direction to give a cell spacing of 22.5 de-

grees. This azimuthal splitting allows for the existence of non-axisymmetric instabilities (such as radiatively driven warps) which may occur due to either physical or numerical effects, while ensuring the calculation remains tractable. The AMR grid was constructed using a maximum mass per cell of 3.0×10^{25} g and a density splitting condition of $f_{\text{split}} = 0.1$. The density in a cylindrical region around the source was reduced to a very low value to ensure that the disc did not completely obscure the source. The radius of this region is $R_{\text{gap}} = 1.0$ au which corresponds to the accretion radius of the SPH sink particle. Two extra levels of grid refinement were added in a box around the central source to ensure that the grid had enough resolution to allow the gap around the source to be resolved. The first box of extra refinement has size 1×10^{14} cm with cells no larger than 1×10^{13} cm and the second box has size 4×10^{13} cm with cells no larger than 4×10^{12} cm.

Monte-Carlo radiative transfer calculations can be computationally demanding so the calculation was parallelised

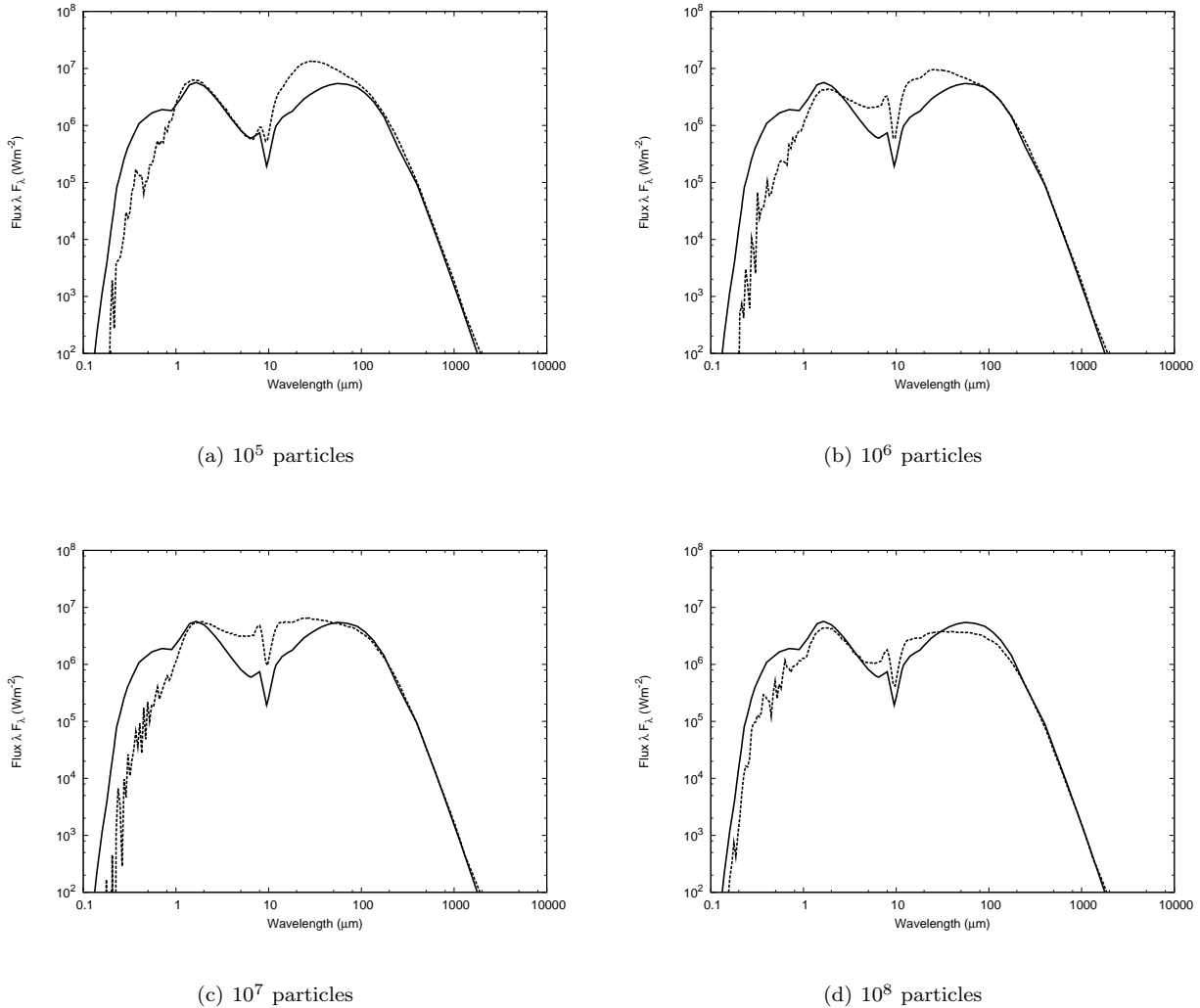


Figure 12. SEDs at a 77.5 degree inclination angle for discs represented by 10^5 , 10^6 , 10^7 and 10^8 particles. The benchmark result is plotted as a solid line and the TORUS SEDs are plotted as dashed lines. The corresponding density distributions in the central part of the disc are plotted in Fig. 8 and fractional temperature errors are plotted in Fig. 9.

using MPI (Message Passing Interface) libraries. Parallelising code in this way allows for parallel computation in both the radiation and hydrodynamics steps and can be applied to a shared memory or a distributed memory computer architecture. The Monte-Carlo calculation dominates the run time of the model but fortunately is very amenable to parallelisation, due to the low communication overhead. The calculations were run on an SGI Altix ICE system using 16 compute nodes, each node comprising two quad core 2.83 GHz Intel Xeon processors. A total of 128 MPI processes were used (one per core). Evolving the disc using both the radiation and hydrodynamics codes took a total wall time of 560 hours of which 440 hours was spent in radiation calculations. The radiation calculations take approximately four times as long as the hydrodynamics calculations so the combined code is significantly slower than the SPH code alone. However the calculation is still feasible and we expect the combined code only to be used in applications where the increased accuracy of the Monte-Carlo radiation calcu-

lation, over faster alternatives such as flux-limited diffusion, is of importance.

5.2 Results

Plots of the disc internal energy are shown in Fig. 13 at six different times during the simulation. As these plots are in cylindrical polar co-ordinates, with different scales on the r and z axes, they have been shown as particle plots, rather than kernel integrated plots. Figure 13(a) shows the initial state before the radiative transfer is switched on when there is a vertically isothermal equation of state. The second frame (Fig. 13(b)) is shortly after the radiative transfer has been switched on. The inner disc has collapsed and there is heating seen in parts of the disc exposed to radiation from the central star. In Fig. 13(c) a scale height enhancement is present in the disc at a radius of approximately 20 au which shadows the region immediately behind causing it to cool. Figure 13(d) shows several such scale height enhancements

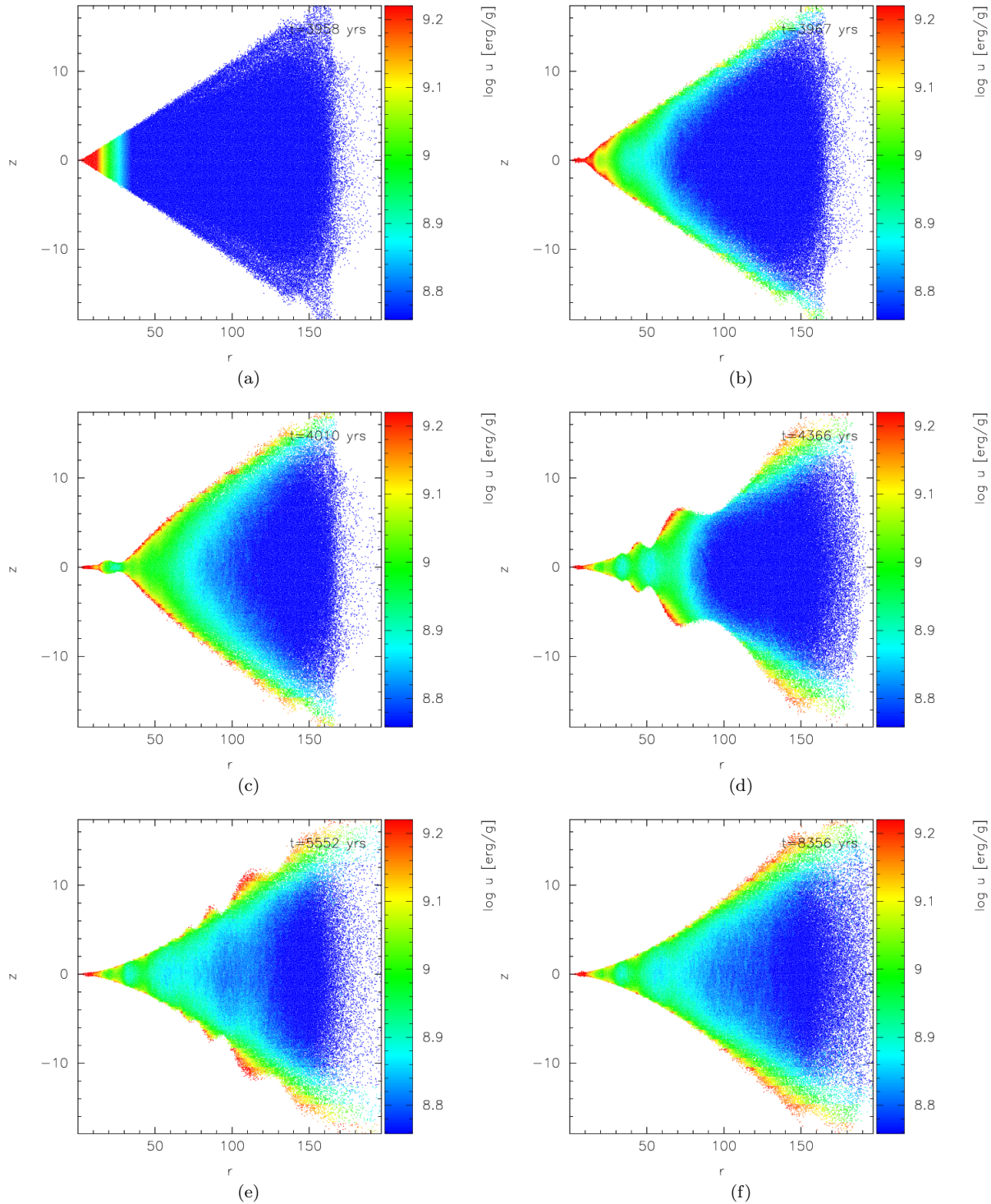


Figure 13. Internal energy distribution in the model disc at six different times as the disc adjusts towards equilibrium. Figure 13(a) shows the initial vertically isothermal state and Fig. 13(f) shows the steady state in hydrostatic and radiative equilibrium. Intermediate frames show the effect of scale height fluctuations on the internal energy within the disc. Internal energy is plotted for each particle in a cylindrical polar co-ordinate system and the axis units are au.

and in each case there is cooling behind the enhancement as the scale height fluctuations are able to affect the mid-plane temperature due to vertical transport of radiation. In Fig. 13(e) the inner region of the disc, within approximately 75 au, has settled and scale height enhancements are seen

only in the outer disc, implying an equilibrium time of order 1600 years at 75 au. As the equilibrium time scales with radius as $r^{\frac{3}{2}}$ we expect the equilibrium time at 150 au to be of order 4500 years. By the last frame (Fig. 13(f)) the majority of the disc has reached a steady state in hydrostatic

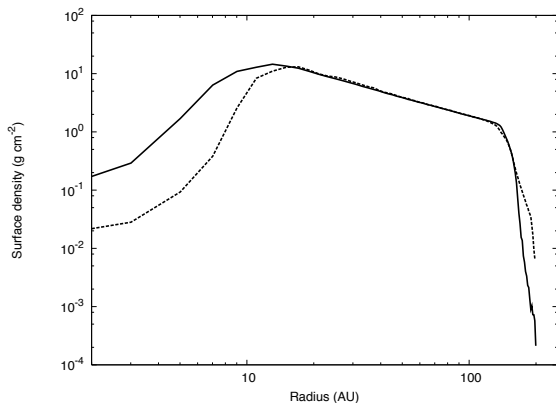


Figure 14. Surface density as a function of radius for the model disc. The solid line is the vertically isothermal disc prior to the radiative transfer code being switched on. The dotted line in shows the disc once it has reached a state of hydrostatic and radiative equilibrium.

and radiative equilibrium, indicating that it is not subject to radiative-hydrodynamic instabilities.

Transient oscillations, as the disc adjusts towards equilibrium, are observed whether radiative transfer is included or not. They are vertical motions which decay more rapidly at smaller radii and hence give the appearance of propagating outwards, even though the motion is vertical. Other disc models using radiation hydrodynamics have found oscillatory solutions with inwards propagating waves (e.g. Min et al. 2009) which are fundamentally different to the transient effects seen in this case. However it should be noted that Min et al. (2009) only found an oscillatory solution in their most optically thick disc, which is significantly more massive than our model disc, and may represent a different regime to that considered here. We note that the disc retains its azimuthal symmetry throughout the simulation and we find no evidence for warping instabilities.

The surface density of the disc is shown in Fig. 14, the scale height is shown in Fig. 15 and the radial temperature profile is shown in Fig. 16. The solid lines are from the vertically isothermal disc shown in Fig. 13(a) and the dotted lines are the disc at the final time step shown in Fig. 13(f). The scale height of the disc was determined by allocating particles to 100 radial bins and fitting a Gaussian to the vertical density profile; the scale height is taken to be the standard deviation of the fitted Gaussian. The radial temperature profile is the average temperature within one scale height of the mid-plane for each radial bin. The majority of the surface density profile is well represented by a power law and does not change significantly as a result of including radiative transfer. Figures 15 and 16 show that the disc is hotter close to the mid-plane, except within a region between 10–20 au of the centre, but has a smaller scale height. Figure 13 shows that the vertical temperature gradient in the disc is such that temperature increases with height out of the mid-plane. Although the disc is hotter when radiative transfer is included the vertical temperature gradient tends to reduce the pressure gradient which is required for hydro-

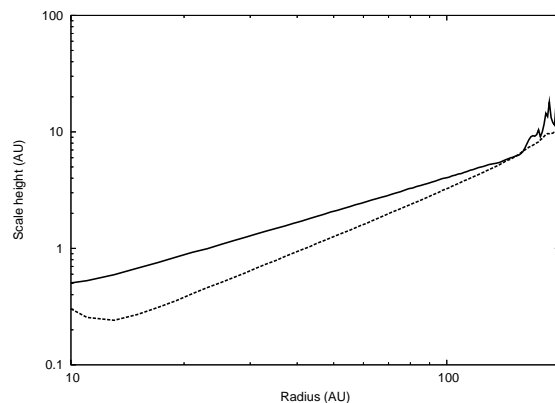


Figure 15. Scale height of the model disc as a function of radius. The solid line is the vertically isothermal disc prior to the radiative transfer code being switched on. The dotted line in shows the disc once it has reached a state of hydrostatic and radiative equilibrium.

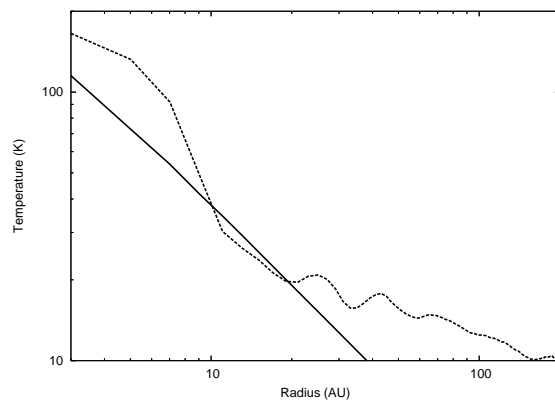


Figure 16. Average temperature within one scale height of the mid plane as a function of radius for the model disc. The solid line is the vertically isothermal disc prior to the radiative transfer code being switched on. The dotted line in shows the disc once it has reached a state of hydrostatic and radiative equilibrium.

static support resulting in a smaller scale height. A slight drop in scale height is evident, just outwards from the disc inner edge, which is indicative of a puffed-up inner edge. Dullemond et al. (2001) find such a puffed-up inner edge when the disc is truncated by dust sublimation. Although the inner edge in our model is not due to dust sublimation, and is found at a greater radius than the Dullemond et al. (2001) case, we are still seeing a puffed up inner edge due to irradiation of an optically thick inner rim.

A notable feature in the surface density plot is the drop in surface density at small radii. This is due to the accretion of material by the central sink particle and will tend to move the optically thick inner edge out to larger radii. Figure 17 shows the SPH density in the central region of the disc at the

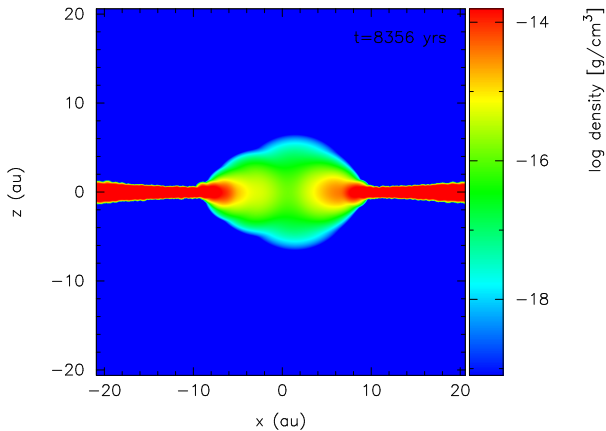


Figure 17. Kernel integrated plot of SPH density in the central region of the disc. This plot is from the last time step of the simulation and shows that the inner edge of the disc has moved outwards from its initial location at 1 au due to the accretion of material by the sink particle.

last time step of the simulation. The inner edge of the disc has moved outwards from its initial value of 1 au. For the purposes of this model we still have an optically thick edge which will shadow the disc but the use of an accreting sink particle is likely to be inappropriate if the exact location of the disc inner edge needs to remain fixed.

6 CONCLUSIONS

We have presented results from a hybrid SPH and AMR grid-based radiative transfer code, which has been used to model a non-self gravitating circumstellar disc. Validation tests of the method have revealed a number of factors which must be taken into consideration when setting up a model of this type.

Although we have found a method for constructing an AMR grid from SPH particles which is robust, in terms of the total mass on the grid, we found that it was necessary to add additional grid refinement in the central region of the disc to allow the inner edge to be well represented. The inner edge of the disc has a large effect on the temperature distribution in the disc and on the emergent SEDs. Consequently the accuracy of the solution is dependent upon the accurate representation of a region which constitutes a small fraction of the disc by volume. As the method combines both SPH and grid elements it is important that both these components have sufficient resolution to represent the disc inner edge. This presents a particular challenge for a SPH code which uses equal mass particles but is achievable with a large number of particles. Accurately modelling the SED using this method is considerably more demanding than accurately representing the temperature structure within the disc. Temperature errors can be reduced to a manageable level using a realistic number of SPH particles, yielding a temperature distribution suitable for use in a hydrodynamics calculation, however even with a disc composed of 10^8

SPH particles the modelled SEDs show significant deviations from the benchmark results.

The combined SPH-radiative transfer code was able to evolve a circumstellar disc to a state of radiative and hydrostatic equilibrium. As the disc settles towards an equilibrium state, vertical motions are seen which give the appearance of an outward propagating scale height fluctuation. This is a vertical motion which decays more rapidly at smaller radii and is seen whether radiative transfer is included or not. These are not the same as the instabilities seen in other radiation hydrodynamics disc models (Min et al. 2009). One consequence of these fluctuations is that they can intercept radiation from the central star which can then be vertically transported into the mid-plane of the disc hence even though the fluctuations are of a small amplitude they exert an influence on the mid-plane temperature.

ACKNOWLEDGMENTS

Calculations presented here were performed using the University of Exeter Supercomputer. DMA was funded by EPSRC grant EP/F011326/1. DAR is funded by an STFC studentship. We thank Matthew Bate for useful discussions. We would like to thank an anonymous referee for helpful comments.

REFERENCES

- Bate M. R., 2009a, MNRAS, 392, 590
- Bate M. R., 2009b, MNRAS, 392, 1363
- Bate M. R., Bonnell I. A., 2005, MNRAS, 356, 1201
- Bate M. R., Bonnell I. A., Bromm V., 2003, MNRAS, 339, 577
- Boss A. P., 1997, Science, 276, 1836
- Boss A. P., 2008, ApJ, 677, 607
- Dullemond C. P., Dominik C., Natta A., 2001, ApJ, 560, 957
- Dullemond C. P., Hollenbach D., Kamp I., D’Alessio P., 2007, in B. Reipurth, D. Jewitt, & K. Keil ed., Protostars and Planets V Models of the Structure and Evolution of Protoplanetary Disks, pp 555–572
- Gingold R. A., Monaghan J. J., 1977, MNRAS, 181, 375
- Goodwin S. P., Whitworth A. P., Ward-Thompson D., 2004, A&A, 414, 633
- Harries T. J., 2000, MNRAS, 315, 722
- Kurosawa R., Harries T. J., Bate M. R., Symington N. H., 2004, MNRAS, 351, 1134
- Kurosawa R., Hillier D. J., 2001, A&A, 379, 336
- Lucy L. B., 1999, A&A, 344, 282
- Masunaga H., Miyama S. M., Inutsuka S.-I., 1998, ApJ, 495, 346
- Min M., Dullemond C. P., Dominik C., de Koter A., Hovenier J. W., 2009, A&A, 497, 155
- Monaghan J. J., 1992, ARA&A, 30, 543
- Nayakshin S., Cha S., Hobbs A., 2009, MNRAS, 397, 1314
- Offner S. S. R., Klein R. I., McKee C. F., Krumholz M. R., 2009, ApJ, 703, 131
- O’Sullivan M., Truss M., Walker C., Wood K., Matthews O., Whitney B., Bjorkman J. E., 2005, MNRAS, 358, 632

- Pascucci I., Wolf S., Steinacker J., Dullemond C. P., Henning T., Niccolini G., Woitke P., Lopez B., 2004, *A&A*, 417, 793
- Pinte C., Harries T. J., Min M., Watson A. M., Dullemond C. P., Woitke P., Ménard F., Durán-Rojas M. C., 2009, *A&A*, 498, 967
- Price D. J., 2007, *PASA*, 24, 159
- Price D. J., 2008, *Journal of Computational Physics*, 227, 10040
- Price D. J., Bate M. R., 2007, *MNRAS*, 377, 77
- Price D. J., Monaghan J. J., 2007, *MNRAS*, 374, 1347
- Rundle D. A., Harries T. J., 2009, In preparation
- Stamatellos D., Whitworth A. P., 2009, *MNRAS*, 400, 1563
- Stamatellos D., Whitworth A. P., Boyd D. F. A., Goodwin S. P., 2005, *A&A*, 439, 159